

Measurement of differential and angle-integrated cross sections for the $^{10}\text{B}(n, \alpha)^7\text{Li}$ reaction from 0.3 eV to 3.0 MeV at CSNS Back-n*

Wenkai Ren (任文凯)¹ Han Yi (易晗)^{2,3} Haofan Bai (白浩帆)¹ Jie Liu (刘杰)¹ Kang Sun (孙康)^{2,3}
 Wei Jiang (蒋伟)^{2,3} Zepeng Wu (邬泽鹏)¹ Cong Xia (夏聪)¹ Guohui Zhang (张国辉)^{1†}
 Yonghao Chen (陈永浩)^{2,3} Ruirui Fan (樊瑞睿)^{2,3} Qiwen Fan (樊启文)⁴ Shixiang Peng (彭士香)¹
 Wentian Cao (曹文田)¹ Tieshuan Fan (樊铁栓)¹

¹State Key Laboratory of Nuclear Physics and Technology, Institute of Heavy Ion Physics, Peking University, Beijing 100871, China

²Institute of High Energy Physics, Chinese Academy of Sciences, Beijing 100049, China

³Spallation Neutron Source Science Center, Dongguan 523803, China

⁴China Institute of Atomic Energy, Beijing 102413, China

Abstract: In the present work, new measurements of differential and angle-integrated cross sections for the $^{10}\text{B}(n, \alpha_1)^7\text{Li}^*$, $^{10}\text{B}(n, \alpha_0)^7\text{Li}$ and $^{10}\text{B}(n, \alpha)^7\text{Li}$ reactions were performed at CSNS Back-n white neutron source. The Light-charged Particle Detector Array (LPDA) system was used to detect the charged particles. The ^6Li -Si monitor was employed to measure the neutron flux. The differential cross sections for the $^{10}\text{B}(n, \alpha)^7\text{Li}$ reaction were obtained from 20.2° to 158.7° (13 angles) in the neutron energy region from 0.3 eV to 3.0 MeV (70 energy points). The differential cross sections for the $^{10}\text{B}(n, \alpha_0)^7\text{Li}$ and $^{10}\text{B}(n, \alpha_1)^7\text{Li}^*$ reactions were also obtained at the same angular positions in the neutron energy region from 0.3 eV to 1.0 MeV (65 energy points). Fitting with the Legendre polynomial series, the angle-integrated cross sections of these three reactions were obtained through integration. The experimental data for these three reactions across such a wide neutron energy range are valuable references for future nuclear data evaluations.

Keywords: $^{10}\text{B}(n, \alpha)^7\text{Li}$, differential cross section, angle-integrated cross section, nuclear data

DOI: 10.1088/1674-1137/ae5dae

CSTR: 32044.14.ChinesePhysicsC.CPC-2026-0107

I. INTRODUCTION

Neutron induced ^{10}B reaction is one of the most important reactions in the nuclear engineering, such as in neutron detection, reactor control, boron neutron capture therapy (BNCT), etc. [1]. In addition, the study of $n + ^{10}\text{B}$ system can enhance the understanding of nuclear reaction mechanism in light nuclei [2]. In the neutron energy region below 1 MeV, the $^{10}\text{B}(n, \alpha)^7\text{Li}$ reaction is the dominate reaction among neutron induced ^{10}B reactions, which can be further divided into $^{10}\text{B}(n, \alpha_0)^7\text{Li}$ ($Q = 2.79$ MeV) and $^{10}\text{B}(n, \alpha_1)^7\text{Li}^*$ ($Q = 2.31$ MeV) reactions corresponding to the ground state and the first excited state of the residual nuclei ^7Li . In the neutron energy region from thermal to 1 MeV, the cross sections of the $^{10}\text{B}(n, \alpha)^7\text{Li}$ and $^{10}\text{B}(n, \alpha_1)^7\text{Li}^*$ reactions have been adopted as the standard cross sections [3]. However, in the MeV energy region and above, discrepancies exist among the results of different measurements and evaluations, because

of the small cross sections, strong background interference and mutual interference between the $^{10}\text{B}(n, \alpha_0)^7\text{Li}$ and $^{10}\text{B}(n, \alpha_1)^7\text{Li}^*$ reactions. Accurate differential cross-section data are essential for nuclear technology applications. Therefore, high-precision measurements are demanded.

For neutron energy $E_n \leq 1.0$ MeV, although numerous measurements of the $^{10}\text{B}(n, \alpha)^7\text{Li}$ reaction have been conducted since 1954 [4], only four measurements of angular distribution and differential cross sections of the $^{10}\text{B}(n, \alpha)^7\text{Li}$ reaction (i. e. Sealock [5], Stelts [6], Hambach [2] and Haoyu Jiang [7]) can be found in EXFOR [4]; and for $1.0 < E_n \leq 3.0$ MeV, only two measurements of differential cross sections (Haoyu Jiang [7] and T.N.Massey [8]) for this reaction can be found in EXFOR [4]. In 2019, our team (Haoyu Jiang et al. [7]) published the differential and angle-integrated cross sections of the $^{10}\text{B}(n, \alpha)^7\text{Li}$ reaction in the neutron energy range from 1.0 eV to 2.5 MeV measured at the China Spallation Neutron

Received 10 February 2026; Accepted 8 April 2026

* The present work was financially supported by the National Natural Science Foundation of China (12475299) and the Key Laboratory of Nuclear Data foundation (JCKY2025201C153)

† E-mail: guohuizhang@pku.edu.cn

©2026 Chinese Physical Society and the Institute of High Energy Physics of the Chinese Academy of Sciences and the Institute of Modern Physics of the Chinese Academy of Sciences and IOP Publishing Ltd. All rights, including for text and data mining, AI training, and similar technologies, are reserved.

Source (CSNS) [9] Back streaming white neutron source (Back-n) [10,11]. The measurement used 15 silicon detectors with angle positions ranging from 19.2° to 160.8° to detect the charged particles. Under the same experimental conditions, our team (Huaiyong Bai *et al.* [12]) have also measured differential and angle-integrated cross sections of the ${}^6\text{Li}(n, t){}^4\text{He}$ reaction, which have been used in the evaluations of the standard cross sections. To reduce the uncertainties introduced from the neutron flux, our team (Jie Liu *et al.* [13]) reanalyzed the measurement data and obtained the ratios of the differential and angle-integrated cross sections of the ${}^{10}\text{B}(n, \alpha){}^7\text{Li}$ reaction over the ${}^6\text{Li}(n, t){}^4\text{He}$ reaction. Analysis shows that the relative uncertainties of these ratios are primarily contributed from the uncertainties in results of the ${}^{10}\text{B}(n, \alpha){}^7\text{Li}$ reaction. Taking these factors into consideration, new and accurate measurements of differential and angle-integrated cross sections for the ${}^{10}\text{B}(n, \alpha){}^7\text{Li}$ reaction are necessary.

In the present work, new measurements of relative differential and angle-integrated cross sections were performed for the ${}^{10}\text{B}(n, \alpha_1){}^7\text{Li}^*$, ${}^{10}\text{B}(n, \alpha_0){}^7\text{Li}$ and ${}^{10}\text{B}(n, \alpha){}^7\text{Li}$ reactions at CSNS Back-n white neutron source with optimized experimental conditions including thinner samples, thinner backing, stronger neutron fluences and simultaneous monitoring of the neutron flux using the ${}^6\text{Li}(n, t){}^4\text{He}$ reaction. In the remaining part of this paper, Section II briefly introduces the experimental setup. Section III presents the data analysis processes, and Section IV reports the results and conclusions.

II. EXPERIMENTAL SETUP

The experiment was performed at EndStation#1 of the CSNS Back-n white neutron source in 2024. As shown in the sketch in Fig. 1, the experimental setup includes three components: the neutron source, the ${}^{10}\text{B}$ samples and the charged particle detectors (including the ${}^6\text{Li}$ -Si monitor and the Light-charged Particle Detector Array (LPDA) system).

A. Neutron Source

The CSNS Back-n white neutrons was generated by a proton beam (1.6 GeV) bombarding a tungsten target,

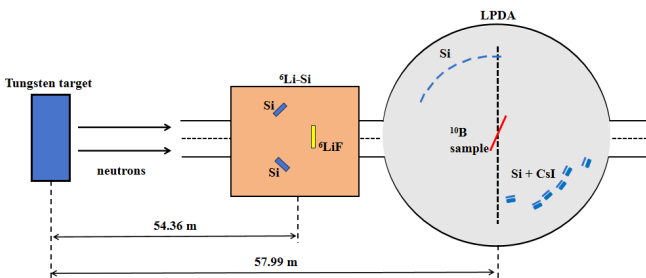


Fig. 1. (color online) The sketch of the experimental setup.

with neutron energy range spanning from 0.3 eV to 300 MeV [11]. The repetition rate of the beam pulse was 25 Hz, the full width at half maximum (FWHM) of the pulse was ~ 70 ns and the interval between the double proton bunches was 410 ns [14]. During the present experiment, the beam power was ~ 160 kW. The flight path from the spallation target to the samples was 57.99 m. In the End-Station#1 of the CSNS Back-n white neutron source, there are three configuration of the shutter and the Collimator-1. To achieve a balance between high count rates and low background interference, the intermediate configuration of $\text{O}50$ mm (shutter) + $\text{O}15$ mm (collimator 1) [15] was selected. In contrast to the largest ($\text{O}50$ mm (shutter) + $\text{O}50$ mm (collimator 1)) and smallest ($\text{O}12$ mm (shutter) + $\text{O}15$ mm (collimator 1)) configurations, this intermediate setup is less commonly used, and its neutron flux data have not been previously published. Under this selected configuration, the neutron beam spot size is approximately 22 mm. Since the present measurement was performed under double-bunch mode [16], the unfolding process is necessary in the data analysis.

B. Samples

Two enriched (90%) ${}^{10}\text{B}$ samples were used back-to-back plated on an aluminum backing $10\ \mu\text{m}$ in thickness. The data of the samples are presented in Table 1, and the pictures are shown in Fig. 2. In additions, an aluminum sheet $10\ \mu\text{m}$ in thickness without samples were also used for background measurement. The LPDA sample holder has four sample positions. The ${}^{241}\text{Am}$ α sources (for energy calibration of the detection system), the ${}^{10}\text{B}$ samples and the aluminum sheet were installed at different sample

Table 1. Sample characteristics

Sample position	Sample	Thickness ($\mu\text{g}/\text{cm}^2$)	diameter (mm)
Forward	${}^{10}\text{B}$	69.5	50
Backward	${}^{10}\text{B}$	73.0	50

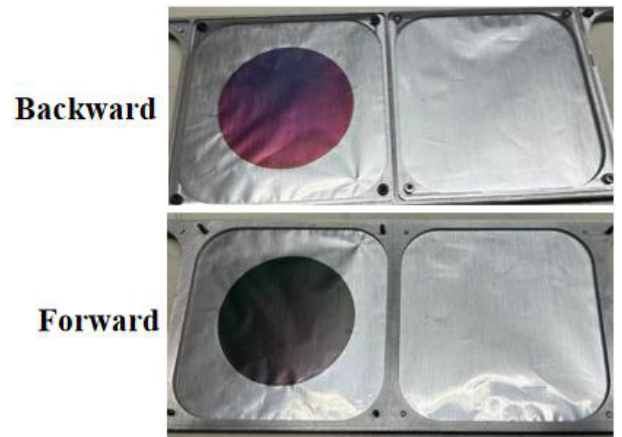


Fig. 2. (color online) The pictures of the ${}^{10}\text{B}$ samples.

positions [7].

C. Charged particle detectors and data

acquisition system

As shown in Fig. 1, a ^6Li -Si [17] monitor (an array of silicon detectors together with a ^6LiF sample) inside the neutron tube was used to measure the relative neutron flux through the $^6\text{Li}(n, t)^4\text{He}$ reaction. A ^6LiF sample ($\sim 350 \mu\text{g}/\text{cm}^2$ in thickness, $\sim 90\%$ in enrichment, 60 mm in diameter) deposited on a 10 μm thick aluminum backing film was used. The neutron attenuation of the aluminum backing film is less than 0.15% [17]. This ^6Li -Si monitor consists of the ^6LiF sample and the 8 silicon detectors each with a thickness of 300 μm and a sensitive area of 20 mm \times 20 mm. The eight silicon detectors are isotropically distributed around the ^6LiF sample at 135° relative to the beam direction.

The Light-charged Particle Detector Array (LPDA) system [18] was used to detect charged particles, as shown in Fig. 1. In the present work, 13 individual silicon detectors (25 mm \times 25 mm \times 300 μm) were implemented, comprising six forward detectors and seven backward detectors, which could cover the particle emission angle from 20.2° to 160.8° . In addition, six cesium iodide scintillator (CsI(Tl)) detectors were also installed behind the six forward silicon detectors intending to measure the events of the $^{10}\text{B}(n, t\alpha)$ reaction. The distributions of the receiving angles of the 13 silicon detectors with respect to the ^{10}B samples are shown in Fig. 3 and their solid angles were (0.00792 \sim 0.0289) sr according to Monte Carlo simulations using Geant4 code [19]. The uncertainties of the receiving angles were obtained by fitting each curve with a Gaussian function. Signals from the ^6Li -Si monitor and LPDA detectors were delivered to the Back-n general purpose data acquisition system (DAQ) [20] for data acquisition.

In the present experiment, the measurements of the ^{10}B samples and the aluminum backing sheet were conducted alternately, and the ratio of their measurement durations was about 3:1. The beam duration for each turn was ~ 24 h, and the total beam duration was ~ 240 h.

III. DATA ANALYSIS

The differential cross sections of the $^{10}\text{B}(n, \alpha)^7\text{Li}$ reaction can be calculated by

$$\begin{aligned} \frac{d\sigma}{d\Omega}(E_n, \theta_{\text{lab}}) &= \varepsilon_{\text{nor}} \cdot \frac{d\sigma}{d\Omega}(E_n, \theta_{\text{lab}})_{\text{relative}} \\ &= \varepsilon_{\text{nor}} \cdot \frac{N_\alpha(E_n, \theta_{\text{lab}})}{I(E_n) \cdot N_c \cdot \Delta\Omega \cdot \varepsilon_d}, \end{aligned} \quad (1)$$

where E_n is the neutron energy, θ_{lab} is the emission angle of the α particle in the laboratory reference system,

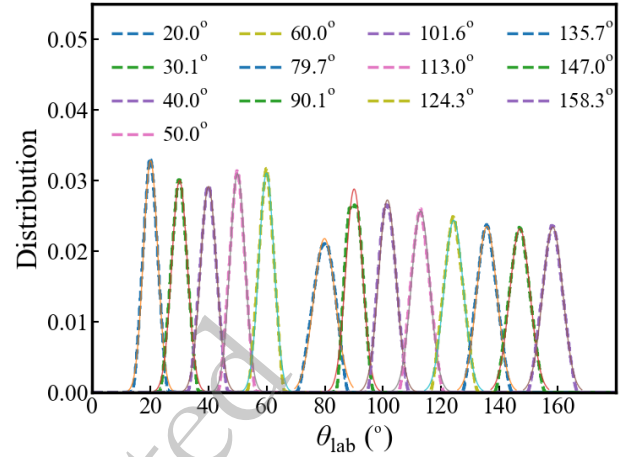


Fig. 3. (color online) The simulated distributions of the receiving angles of the silicon detectors.

$N_\alpha(E_n, \theta_{\text{lab}})$ is the number of the counts of the α particles in an energy bin centered at E_n and in the angle bin centered at θ_{lab} , $I(E_n)$ is the relative neutron fluence in each neutron energy bin, N_c is the ^{10}B atom number in the sample, $\Delta\Omega$ is the solid angle of each silicon detector in the LPDA, ε_d is the detection efficiency of each silicon detector. Due to the lacking of the absolute neutron fluence and the non-uniformity correction of the neutron beam, the normalization factor (ε_{nor}) was determined in the neutron energy range from 0.5 eV to 1.5 eV, based on the evaluated data from IAEA-Std17 [3], which are the consistent with those in the ENDF-B/VIII.1 [21].

The values of θ_{lab} and $\Delta\Omega$ have been obtained in Sec. II.C, and the ^{10}B atom number N_c can be calculated from the data presented in Table 1. The E_n was determined by the time-of-flight (TOF) method. The uncertainty of E_n was mainly attributed to the width of the proton beam pulse. The $N_\alpha(E_n, \theta_{\text{lab}})$ was obtained through analyzing the measured LPDA data from the ^{10}B samples which will be shown in Sec. III.A. The values of ε_d were obtained through the comparison between the spectra from measurements and the simulations. The $I(E_n)$ was obtained through analyzing the data from the ^6Li -Si monitor. In the present work, relative differential cross sections were obtained firstly, and then relative angle-integrated cross sections were calculated with the Legendre polynomial fitting. Finally, the normalization factor (ε_{nor}) was calculated using the standard cross sections of the $^{10}\text{B}(n, \alpha)^7\text{Li}$ reaction in the 0.5 \sim 1.5 eV region.

A. Determination of the numbers of the $^{10}\text{B}(n, \alpha)^7\text{Li}$, $^{10}\text{B}(n, \alpha_0)^7\text{Li}$ and $^{10}\text{B}(n, \alpha_1)^7\text{Li}^*$ events

A typical E_n -Amplitude (the amplitude of the signals from the Si detectors) two-dimensional spectrum at 30.1° is shown in Fig. 4(a), where the α_0 , α_1 and ^7Li events are clearly shown. The simulated E_n -Amplitude two-dimensional spectrum at the same angle position is shown in

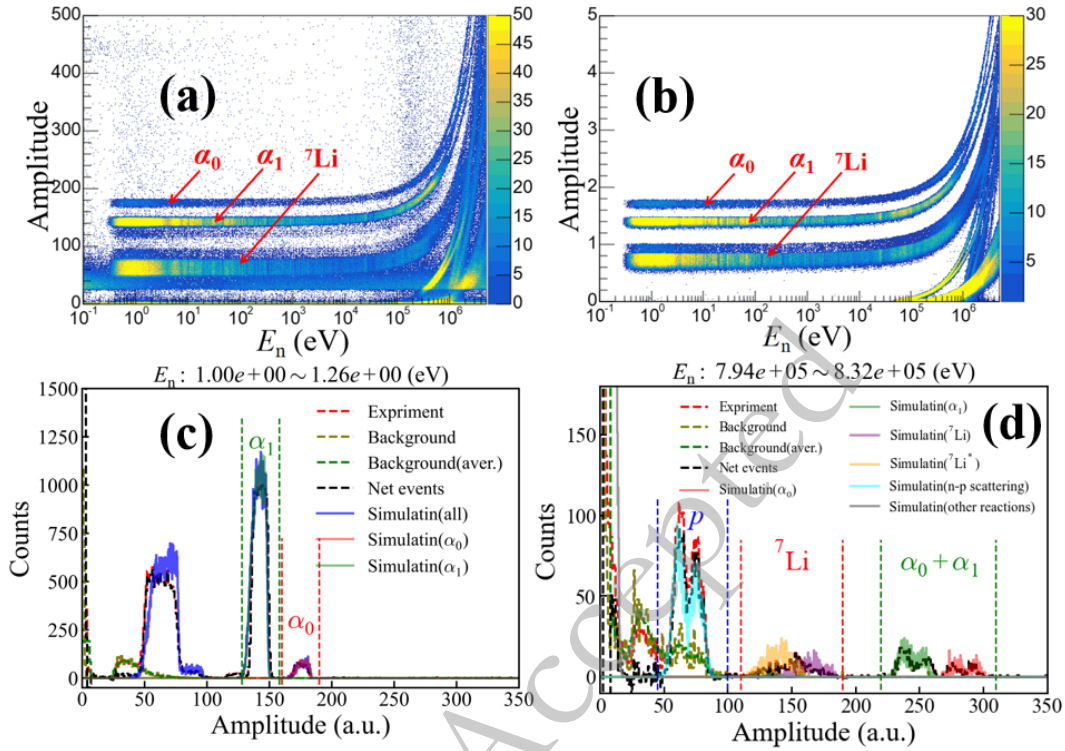


Fig. 4. (color online) The measured E_n -Amplitude two-dimensional spectrum at the angle position of 30.1° (a), the simulated E_n -Amplitude two-dimensional spectrum at the angle position of 30.1° (b), the experimental PHS and the simulated PHS in the neutron energy bin from 1.00 eV to 1.26 eV (c) and those in the neutron energy bin from 794 keV to 832 keV (d) at 30.1° .

Fig. 4 (b). The simulation was performed using Geant4 code [19], and 7 reaction channels were considered, including $^{10}\text{B}(n, \alpha_0)^7\text{Li}$, $^{10}\text{B}(n, \alpha_1)^7\text{Li}^*$, $^{10}\text{B}(n, p)$ ($Q = 0.23$ MeV), $^{10}\text{B}(n, t2\alpha)$ ($Q = 0.322$ MeV), $^{10}\text{B}(n, n)^{10}\text{B}$, n-p scattering, and $^{27}\text{Al}(n, \alpha)^{24}\text{Na}$ ($Q = -3.132$ MeV) reactions. The evaluated values of the cross sections and angular distributions from the ENDF/B-VIII.1 library [21] were used for simulation. Additionally, the double-bunch proton mode with the interval of 410 ns and the ~ 70 ns proton pulse width were also considered. One can see from the simulation result shown in Fig. 4(b), the ^7Li events and the background events from other reactions (such as $^{10}\text{B}(n, p)$, n-p scattering, etc.) rarely interfere with the α_0 and α_1 events for E_n below 3.0 MeV. The α_0 events and α_1 events could be clearly distinguished in the neutron energy region below 1 MeV. However, in the neutron energy region above 1 MeV, both the α_0 and α_1 events originating from the double-bunch proton pulses gradually separate leading to the overlap between α_0 and α_1 events.

The pulse height spectra (PHSs) at different E_n bins were obtained to determine the $N_\alpha(E_n, \theta_{\text{lab}})$ counts. For $E_n < 100$ keV, because the kinetic energies of the emitted α particles remain nearly constant, the measured and simulated PHSs at 10 neutron energy bins per decade (bpd) were obtained, one of which is shown in Fig. 4(c). For $E_n > 100$ keV, in order to enhance energy resolution in the

PHSs, the PHSs at 50 bpd were constructed to determine the counts of α events and to subtract the background, one of the PHSs at 50 bpd is shown in Fig. 4(d). These counts were subsequently re-binned to 10 bpd in order to derive differential cross sections.

The background from both the strong gamma flash and the backing sheet is non-negligible, so background measurement and subtraction are essential. The measured PHSs of the foreground spectra are shown in Figs. 4(c) and (d) by red dashed lines, while the corresponding background spectra are shown by the yellow dashed lines. The neutron fluences were normalized between the background measurement and the $^{10}\text{B}(n, \alpha)^7\text{Li}$ measurement according to the integration of the accelerator proton flux. The experimental background PHSs were smoothed before obtaining the background-subtracted (net) PHSs, with the smoothed background spectra shown by the green dashed lines in Figs. 4(c) and (d). The resulting net spectra are indicated by the black dashed lines in Figs. 4(c) and (d). To identify the $^{10}\text{B}(n, \alpha)^7\text{Li}$, $^{10}\text{B}(n, \alpha_0)^7\text{Li}$ and $^{10}\text{B}(n, \alpha_1)^7\text{Li}^*$ events, the background-subtracted PHSs were compared with the simulated ones, which are shown by the blue, red, and green solid lines in Figs. 4(c) and (d). One can see that the simulated PHSs agrees well with the measured PHSs. These simulations also enabled the determination of the detection efficiencies at various angle positions. In addition, the contribution of ambient-

scattered thermal neutrons to the background is negligible, due to their very low flux (< 10 /cm²/s) [22].

At detection angles bigger than 30.0° , the impact of the background on the α event was very small. Considering that the background was smoothed, one fifth of the background counts was considered as error, and the uncertainty from background subtraction was less than 1%. At the smallest detection angle (20.1°), the background interference was more significant, because the Si detection was near the neutron beam. The uncertainty from background subtraction for the $^{10}\text{B}(n, \alpha_0)^7\text{Li}$ events reaches up to 20% only in a few energy bins above 100 keV, while in most energy bins it remains below 1%. Furthermore, the uncertainty of determination of the valid area for the $^{10}\text{B}(n, \alpha)^7\text{Li}$ and $^{10}\text{B}(n, \alpha_1)^7\text{Li}^*$ events was estimated to be less than 1% in the neutron energy region below 300 keV, and less than 3% in the neutron energy region from 300 keV to 1 MeV. For the $^{10}\text{B}(n, \alpha_0)^7\text{Li}$ events, the uncertainty of determination of the valid area could reach up to 17.5% only in a few energy bins above 300 keV, while in most energy bins it remains below 4%. In several energy bins above 300 keV, the statistical errors and the uncertainty of background subtraction for $^{10}\text{B}(n, \alpha_0)^7\text{Li}$ events become significant, owing to low counts of $^{10}\text{B}(n, \alpha_0)^7\text{Li}$ events and high counts of background. The detection efficiency at each detection angles was found to be approximately 100%.

Due to the 410 ns interval between the double-bunch proton beams, there is a non-negligible error in the determination of neutron energies above 0.02 MeV. For $E_n < 3.0$ MeV, since there is no dense resonance structure in the $^{10}\text{B}(n, \alpha)^7\text{Li}$, $^{10}\text{B}(n, \alpha_0)^7\text{Li}$ and $^{10}\text{B}(n, \alpha_1)^7\text{Li}^*$ cross sections, an iterative method was used for unfolding. This unfolding method has been successfully used in our previous measurements of the $^6\text{Li}(n, t)^4\text{He}$ and $^{10}\text{B}(n, \alpha)^7\text{Li}$ reactions at CSNS Back-n white neutron source [7, 12]. While the double-bunch unfolding effectively reduces neutron energy deviation, it is the most significant source of the uncertainty for the measured differential and angle-integrated cross sections. The deviation before and after the double-bunch unfolding is regarded as the error of the double-bunch unfolding. For differential cross sections the uncertainty introduced from the unfolding process ranges from 0.2% to 19.8%, while for angle-integrated cross sections, the uncertainty ranges from 0.2% to 2.3%. A summary of the uncertainty can be found in Sec. C.

B. Determination of the relative neutron fluence

The ^6Li -Si monitor [17] was used to measure the neutron flux. The relative neutron fluence $I(E_n)$ was calculated from

$$I(E_n) = \varepsilon_{\text{nor}} \frac{N(E_n)}{\frac{d\sigma}{d\Omega}(E_n, \theta_{\text{lab}} = 135^\circ) \cdot \Delta\Omega \cdot N_s}, \quad (2)$$

where $N(E_n)$ is the $^6\text{Li}(n, t)^4\text{He}$ event number in each neutron energy bin, and $\frac{d\sigma}{d\Omega}(E_n, \theta_{\text{lab}} = 135^\circ)$ is the differential cross sections of the $^6\text{Li}(n, t)^4\text{He}$ reaction taken from evaluation data from ENDF/B-VIII.1 [21], JEFF-3.3 [23], and BROND-3.1 [24]. $\Delta\Omega$ is the solid angle of the silicon detector, and N_s is the relative ^6Li atom number in the ^6LiF sample. The N_s has been presented in Sec. II.C, and the $\Delta\Omega$ was obtained by Monte Carlo simulations using Geant4 code [19]. Consistent with Eq. (1), the same normalization factor (ε_{nor}) was used here.

The signals from five silicon detectors, positioned at the same receiving angle of 135° with respect to the ^6LiF sample in the laboratory system (as described in Sec. II.C), were merged and analyzed to enhance statistical accuracy of the neutron fluence. The E_n -Amplitude two-dimensional spectrum measured by the ^6Li -Si monitor after merging is shown in Fig. 5(a), where the triton and α events from the $^6\text{Li}(n, t)^4\text{He}$ reaction are clearly separated at $E_n < 3.0$ MeV. The simulated E_n -Amplitude two-dimensional spectrum is shown in Fig. 5(b). In the neutron energy below 3.0 MeV, the valid-event-area of the triton and α events from the $^6\text{Li}(n, t)^4\text{He}$ reaction can be clearly identified, and the influence of the background is negligible. The primary background sources include neutron-induced reactions from the aluminum backing (e.g., $^{27}\text{Al}(n, p)^{27}\text{Mg}$ ($Q = -1.828$ MeV), $^{27}\text{Al}(n, \alpha)^{24}\text{Na}$ ($Q = -3.132$ MeV) and $^{19}\text{F}(n, \alpha)^{16}\text{N}$ ($Q = -1.525$ MeV) reactions) and the gamma-flash. The gamma-flash effects are minimal due to the large angle placement of the detectors, and background contributions from the aluminum backing are significant only for $E_n > 3.0$ MeV.

To obtain the triton and α count at an energy bin and to determine their detection efficiencies, the experimental PHSs with 10 neutron bins per decade (10 bpd) were compared with the simulated ones. A typical experimental PHS at $E_n < 100$ keV is shown in Fig 5(c), compared with the simulated PHS. The detector efficiency for triton and α events in the neutron energy below 100 keV is nearly 100% from simulation. For $E_n < 100$ keV, the uncertainty of the determination for the valid area and the detector efficiency is less than 0.5%, and the statistical uncertainty of the triton and α events is less than 1.0%. The triton and alpha counts spectra from the double-bunch neutron were unfolded using the iterative method, which is the same method used for the analysis of the ^{10}B data in Sec. III.A. The method of uncertainty calculation is the same as in Sec. III.A, and the uncertainty introduced from the double-brunch unfolding is less than 1.6%.

The differential cross sections of the $^6\text{Li}(n, t)^4\text{He}$ reaction for different neutron energies were taken from the average of the evaluation data from ENDF/B-VIII.1 [21], JEFF-3.3 [23], and BROND-3.1 [24]. The uncertainties of the evaluation data were estimated from the maximum

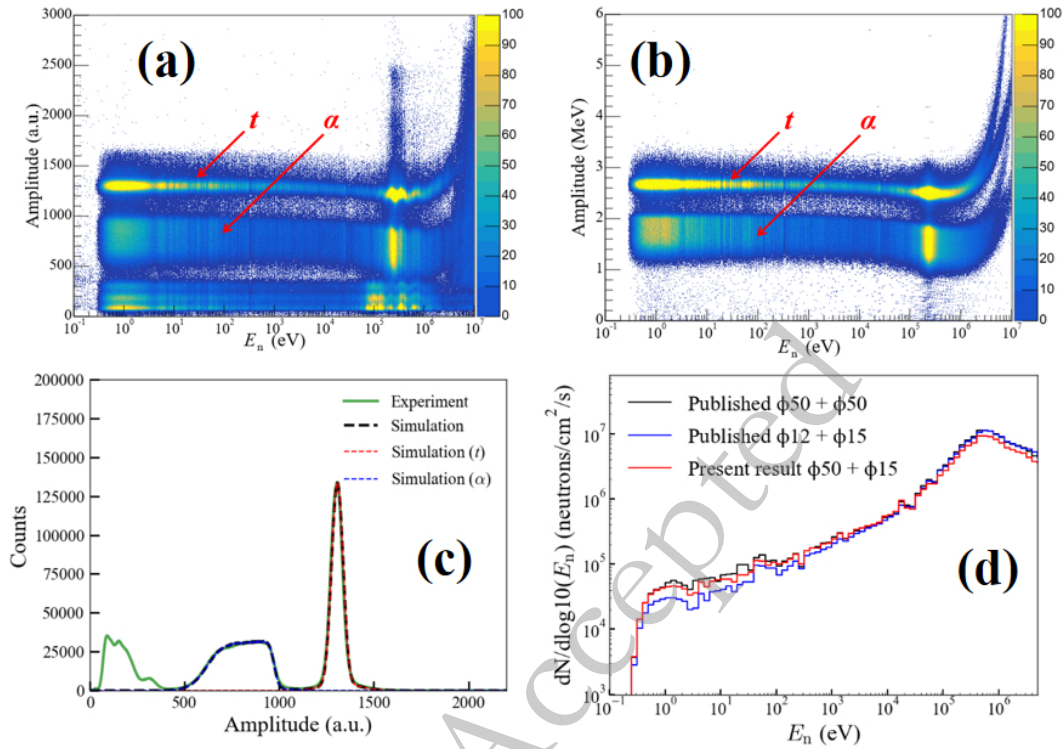


Fig. 5. (color online) The measured E_n -Amplitude two-dimensional spectrum of the ${}^6\text{Li}$ -Si monitor (a), the simulated E_n -Amplitude two-dimensional spectrum (b), the experimental PHS and the simulated PHS at neutron energy below 100 keV (c), and the measured neutron flux with 10 bpd [24,25] (d).

deviation among different datasets. The uncertainties of the evaluated differential cross sections for both triton and α emission at $\theta_{\text{lab}} = 135^\circ$ are less than 0.5% for neutron energies below 1 keV. In the neutron energy range from 1 keV to 100 keV, the uncertainties of the evaluated differential cross sections for triton emission increase from 0.5% to 3.2%, and those for α emission increase from 0.5% to 1.4%. The ε_{nor} was calculated using the neutron flux in the neutron energy from 0.5 eV to 1.5 MeV with a beam configuration of $\varnothing 50$ mm (shutter) + $\varnothing 50$ mm (collimator 1) published in 2024 [25,26], with a normalization uncertainty of $\sim 1.3\%$. In the energy range from 0.3 eV to 100 keV, the neutron flux was calculated using both the counts of triton and α events from Fig. 5(a), according to Eq. (2). The neutron fluxes derived from triton events and from α events show a discrepancy of less than 3.0%. To address the constraint of relying solely on the differential cross sections from a single angle position, a statistically weighted average of the two neutron fluxes derived independently from triton and from α events was employed, with weights determined by their event statistics. The resulting flux was used in Eq. (1), and their uncertainties range from 1.5% to 2.6% for the determination of the differential cross sections of the ${}^{10}\text{B}(n, \alpha){}^7\text{Li}$ reaction.

The pronounced resonance at approximately 0.24 MeV in the excitation function of the ${}^6\text{Li}(n, t){}^4\text{He}$ reac-

tion renders this reaction unsuitable for direct neutron flux measurements at neutron energies above 100 keV. In the neutron energy range from 100 keV to 3.0 MeV, the neutron flux was derived by normalizing the neutron flux with the $\varnothing 50$ mm + $\varnothing 50$ mm configuration to the integral of the flux measured by the ${}^6\text{Li}$ -Si monitor. The final uncertainty, combining the contributions from the published data and normalization, ranges from 1.8% to 2.7%. The measured neutron flux using the ${}^6\text{Li}$ -Si monitor is shown by the red line in Fig 5(d). The black line in Fig. 5(d) represents the published neutron flux data obtained with a beam configuration of $\varnothing 50$ mm (shutter) + $\varnothing 50$ mm (collimator 1), while the blue line corresponds to the configuration of $\varnothing 12$ mm (shutter) + $\varnothing 15$ mm (collimator 1). Compared with the $\varnothing 50$ mm + $\varnothing 50$ mm configuration, the neutron flux measured with $\varnothing 12$ mm + $\varnothing 15$ mm differs more significantly from that of the present experiment ($\varnothing 50$ mm + $\varnothing 15$ mm).

C. Calculation of the differential cross sections and angle-integrated cross sections

According to Eq. (1), the relative differential cross sections were obtained and subsequently fitted using fourth-order Legendre polynomial series. The fitted functions were then integrated to yield the relative angle-integrated cross sections. As shown in Fig. 6, the relative angle-integrated cross sections for the ${}^{10}\text{B}(n, \alpha){}^7\text{Li}^*$ reac-

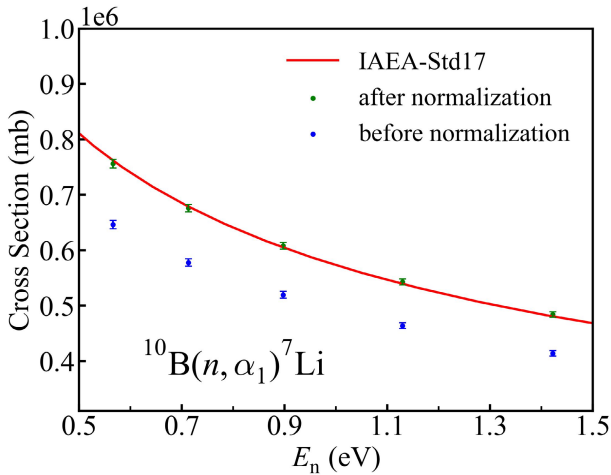


Fig. 6. (color online) The determination of the normalization factor.

tion (the blue points) were normalized to the standard cross section (angle-integrated cross sections) from IAEA-Std17 [3] in the neutron energy range from 0.5 eV to 1.5 eV. This procedure determined the normalization factor ε_{nor} of the present work for both the angle-integrated cross section and the differential cross sections.

The uncertainty of this normalization factor is 1.3%, which accounts for both the uncertainty of the standard cross section and the deviation of cross sections between the normalized results and evaluated values. Table 2 details the sources of the uncertainties and their magnitudes.

The sources of uncertainties for the differential cross sections of the $^{10}\text{B}(n, \alpha_1)^7\text{Li}^*$, $^{10}\text{B}(n, \alpha_0)^7\text{Li}$ and $^{10}\text{B}(n, \alpha)^7\text{Li}$ reactions include the uncertainties of the counts of

events, relative neutron flux, detection solid angles, number of ^{10}B atoms, and normalization factor. Among these, the uncertainties of counts of the $^{10}\text{B}(n, \alpha_1)^7\text{Li}^*$, $^{10}\text{B}(n, \alpha_0)^7\text{Li}$ and $^{10}\text{B}(n, \alpha)^7\text{Li}$ reactions arise from the uncertainties in the statistical error of the valid α events, the unfolding of the double-bunch proton beams, the determination of the valid-even-area, the background subtraction and the detection efficiency. For the differential cross sections of the $^{10}\text{B}(n, \alpha)^7\text{Li}$ and $^{10}\text{B}(n, \alpha_1)^7\text{Li}^*$ reactions, the total uncertainty ranges from 2.4% to 8.7%. For the $^{10}\text{B}(n, \alpha_0)^7\text{Li}$ reaction, the uncertainty ranges from 3.3% to 32.7%, which is mainly because the counts of the $^{10}\text{B}(n, \alpha_0)^7\text{Li}$ reaction are significantly less than the counts of the $^{10}\text{B}(n, \alpha)^7\text{Li}$ and $^{10}\text{B}(n, \alpha_1)^7\text{Li}^*$ reactions. In the neutron energy range below 1 keV, the uncertainties of the differential cross sections for the $^{10}\text{B}(n, \alpha)^7\text{Li}$ and $^{10}\text{B}(n, \alpha_1)^7\text{Li}^*$ reactions primarily come from the uncertainties in normalization, nuclear number, and neutron flux measurements. In contrast, at high neutron energies, statistical error and double-bunch unfolding error are the primary sources of uncertainties. For the $^{10}\text{B}(n, \alpha_0)^7\text{Li}$ reaction, the uncertainties due to statistical errors, double-bunch unfolding, determination of the valid-even-area and background subtraction are larger than those uncertainty of $^{10}\text{B}(n, \alpha)^7\text{Li}$ and $^{10}\text{B}(n, \alpha_1)^7\text{Li}^*$ reactions. The complete differential cross section data of the present work are provided in the Supporting Information file "Differential cross sections.xlsx".

For the angle-integrated cross sections, the uncertainties due to the statistical errors, double-bunch unfolding, determination of the valid-even-area and background subtraction are significantly reduced, while an additional un-

Table 2. Sources of the uncertainties and their magnitudes

Source of uncertainty	Magnitude (%)	
	Differential cross sections	Angle-integrated cross sections
Relative neutron flux	1.5 ~ 3.0	1.5 ~ 3.0
Statistical error of the valid α events	0.5 ~ 5.5 ^a (10.7 ^b)	0.2 ~ 2.6
Unfolding of the double-bunch proton beams	0.5 ~ 5.6 ^a (18.5 ^b)	0.2 ~ 2.8
Determination of the valid-even-area	< 4.0 ^a (< 17.5 ^b)	< 0.6 ^a (< 3.0 ^b)
Background subtraction	< 5.0 ^a (< 22.8 ^b)	< 0.1 ^a (< 1.5 ^b)
Detection efficiency	< 0.1	< 0.1
Number of the ^{10}B atoms	1.0	1.0
Detection solid angle	< 0.4	< 0.4
Legendre polynomial fitting	-	0.2 ~ 6.2
Normalization	1.3	1.3
Total uncertainty of the $^{10}\text{B}(n, \alpha)^7\text{Li}$ reaction	2.4 ~ 8.5	2.4 ~ 7.0
Total uncertainty of the $^{10}\text{B}(n, \alpha_0)^7\text{Li}$ reaction	3.3 ~ 32.7	3.3 ~ 7.9
Total uncertainty of the $^{10}\text{B}(n, \alpha_1)^7\text{Li}$ reaction	2.4 ~ 8.7	2.4 ~ 6.4

a: uncertainties of the $^{10}\text{B}(n, \alpha)^7\text{Li}$ and $^{10}\text{B}(n, \alpha_1)^7\text{Li}^*$ reactions. b: uncertainties of the $^{10}\text{B}(n, \alpha_0)^7\text{Li}$ reaction.

certainty component is introduced by the Legendre polynomial fitting. For the angle-integrated cross sections of the $^{10}\text{B}(n, \alpha)^7\text{Li}$ and $^{10}\text{B}(n, \alpha_1)^7\text{Li}^*$ reactions, the total uncertainty ranges from 2.4% to 7.0%. For the $^{10}\text{B}(n, \alpha_0)^7\text{Li}$ reaction, the uncertainty ranges from 3.3% to 7.9%. The present experimental data of angle-integrated cross sections for the $^{10}\text{B}(n, \alpha_1)^7\text{Li}^*$, $^{10}\text{B}(n, \alpha_0)^7\text{Li}$ and $^{10}\text{B}(n, \alpha)^7\text{Li}^*$ reactions are included in the Supporting Information file "Angle-integrated cross sections.xlsx".

IV. RESULT AND DISCUSSIONS

After the data processing presented in Sec. III, The differential cross sections for the $^{10}\text{B}(n, \alpha)^7\text{Li}$ reaction were obtained from 20.2° to 158.7° (13 angles) in the neutron energy region from 0.3 eV to 3.0 MeV with 10 bpd (70 energy points). The differential cross sections for the $^{10}\text{B}(n, \alpha_0)^7\text{Li}$ and $^{10}\text{B}(n, \alpha_1)^7\text{Li}^*$ reactions were also obtained at the same angular positions in the neutron energy region from 0.3 eV to 1.0 MeV with 10 bpd (65 energy points). The present differential cross sections results are discussed in Sec. IV.A. In addition, the present angle-integrated cross sections for these three reactions

were also obtained in the corresponding neutron energy range, which are discussed in Sec. IV.B.

A. Differential cross sections

Typical measurement results of differential cross sections for $^{10}\text{B}(n, \alpha_1)^7\text{Li}^*$, $^{10}\text{B}(n, \alpha_0)^7\text{Li}$ and $^{10}\text{B}(n, \alpha)^7\text{Li}^*$ reactions are shown in Figs. 7, 8 and 9, respectively. These results are compared with existing data from measurements and evaluations.

In the neutron energy range below 1 keV, the present differential cross sections of these three reactions exhibit a nearly isotropic distribution in the center-of-mass system, consistent with both the evaluations and with the measurements of Haoyu Jiang (2019) [7]. As shown in Figs. 7(a), 8(a) and 9(a), this agreement confirms the reliability of the present experimental results to a certain extent. In Fig. 7(a), the differences between the present results (black points) and the previous results (red points) arise from the difference in neutron energy. According to IAEA-Std17 [3], the $^{10}\text{B}(n, \alpha_1)^7\text{Li}^*$ cross section is 540 b at $E_n = 1.129 \pm 0.004$ eV for the present measurement, compared to 573 b at $E_n = 1.000 \pm 0.004$ eV for the previous measurement.

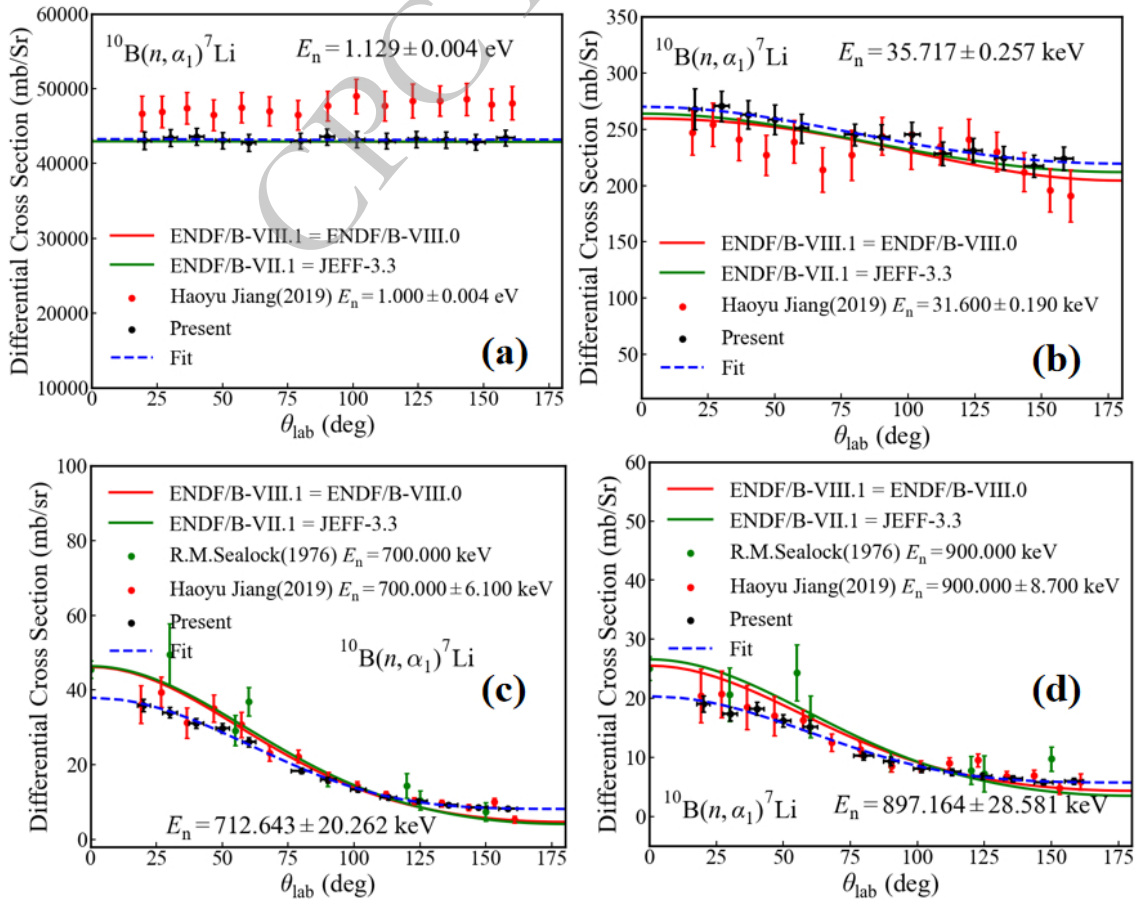


Fig. 7. (color online) Typical differential cross sections of the $^{10}\text{B}(n, \alpha_1)^7\text{Li}^*$ reaction measured in the present work compared with existing results of measurements and evaluations [4, 21, 23, 27, 28].

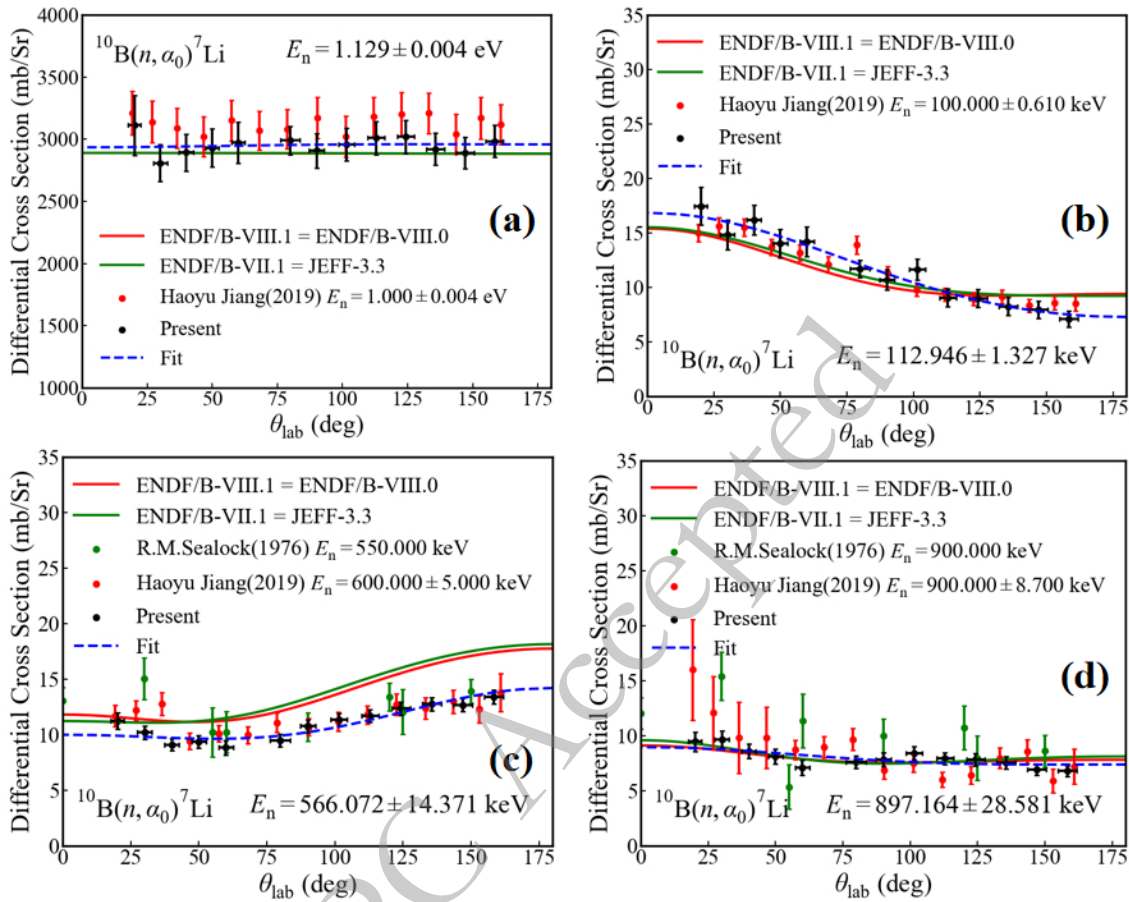


Fig. 8. (color online) Typical differential cross sections of the $^{10}\text{B}(n, \alpha)^7\text{Li}$ reaction measured in the present work compared with existing results of measurements and evaluations [4, 21, 23, 27, 28].

In the neutron energy range from 1 keV to 100 keV, the present differential cross sections of these three reactions exhibit a slight forward bias in the laboratory reference system, due to the effect of nuclear reaction kinetics, as shown in Figs. 7(b) and 9(b). In addition, these results agree well with both the results from evaluations and measurements.

In the neutron energy range from 100 keV to 1 MeV, the present differential cross sections of the $^{10}\text{B}(n, \alpha_1)^7\text{Li}^+$ reaction display a strong forward bias, which are mainly contributed from the $7/2^+$ s -wave state of the compound nucleus ^{11}B [30], as shown in Figs. 7(c), and 7(d). Compared with those from existing measurements, the present results are consistent with the measurement data of Haoyu Jiang (2019) [7]. Noticeable discrepancies are observed between the present data and the measurement data of R.M.Sealock (1974) [5]. Compared to the evaluations, the present results show a similar forward trend, though with smaller magnitudes than those predicted in the evaluation libraries including ENDF/B-VIII.1 [21] and JEFF-3.3 [23]. For the $^{10}\text{B}(n, \alpha_0)^7\text{Li}$ reaction, the present differential cross sections show a strong backward bias at the 0.3 ~ 0.6 MeV region, which are contrib-

uted from the $5/2^-$ p -wave ($E_n \sim 0.52$ MeV) resonance of the compound nucleus ^{11}B [30], as shown in Fig. 8(c). In the 0.6 ~ 1.0 MeV region, the present differential cross sections of the $^{10}\text{B}(n, \alpha_0)^7\text{Li}$ reaction become nearly an isotropic distribution in the laboratory system, as shown in Fig. 8(d). Compared to the measurement results, the present results are consistent with the measurement data of Haoyu Jiang (2019) [7], and are lower than the measurement data of R.M.Sealock (1974) [5] at small angles.

In the neutron energy range of 1.0 MeV ~ 3.0 MeV, the present differential cross sections of the $^{10}\text{B}(n, \alpha)^7\text{Li}$ reaction show a forward-peak behavior, which might be contributed from the resonances of the $9/2^-$ p -wave state ($E_n = 1.83$ MeV) and $5/2^+$ or $7/2^+$ d -wave state ($E_n = 1.88$ MeV) of the compound nucleus ^{11}B [32], as shown in Figs. 9(c) and 9(d). Compared with the data from evaluations, the present results deviate from the evaluated trends in ENDF/B-VIII.1 [21] and CENDL-3.2 [27] libraries, where the differential cross sections decrease monotonically with increasing emission angle, the present experimental results are in best agreement with the data from ENDF/B-VIII.1 [21] among all the evaluated nuclear data libraries. In comparison with previous measure-

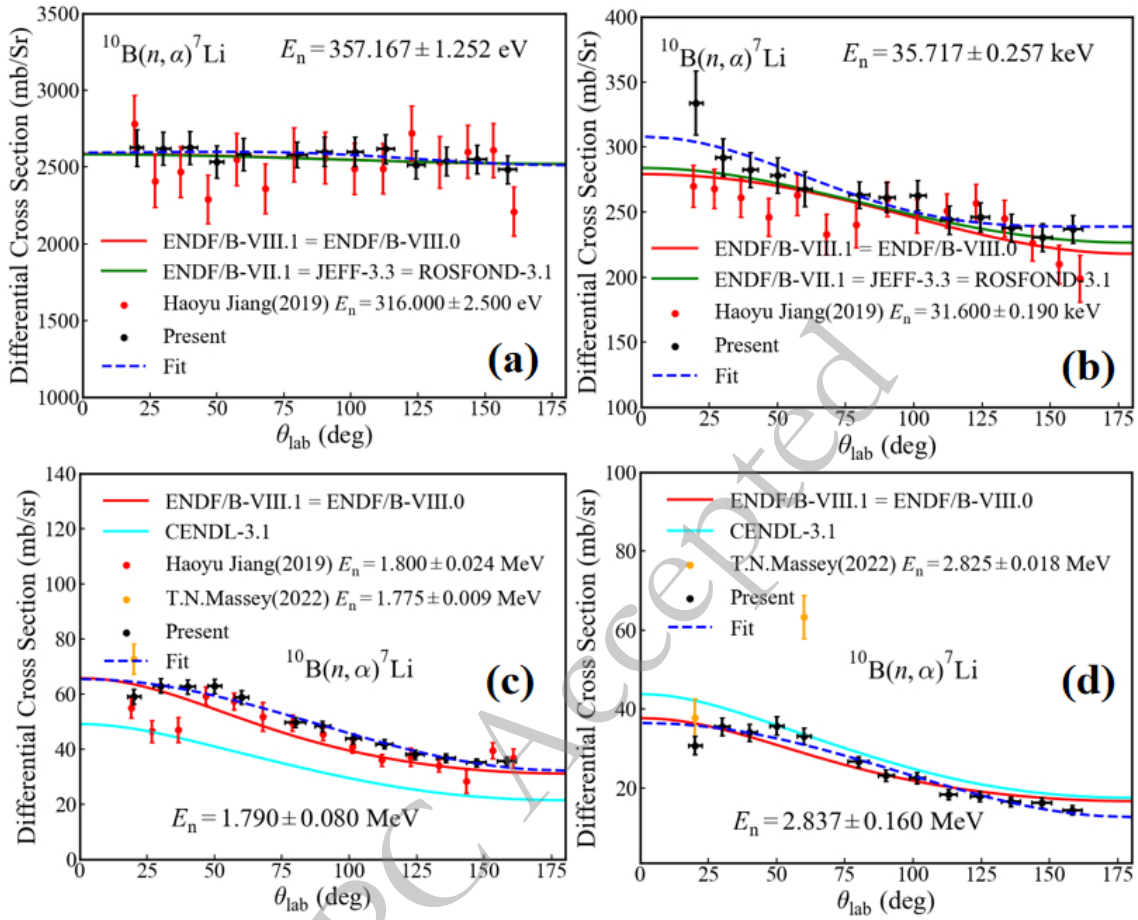


Fig. 9. (color online) Typical differential cross sections of the $^{10}\text{B}(n, \alpha)^7\text{Li}$ reaction measured in the present work compared with existing results of measurements and evaluations [4, 21, 23, 27, 28].

ments, the present differential cross sections of the $^{10}\text{B}(n, \alpha)^7\text{Li}$ reaction at 30.1° and 40.0° are significantly higher than those of Haoyu Jiang(2019) [7], as shown in Fig. 9(c). This might be due to the excessive background noise in the experiments of Haoyu Jiang (2019) [7]. Compared with the results of T.N. Massey (2022) [8], the present data are lower at the forward emission angles, as shown in Fig. 9(d).

In general, the present differential cross sections are consistent with the evaluation data. Compared with existing measurement results of the differential cross sections for the $^{10}\text{B}(n, \alpha_1)^7\text{Li}^*$, $^{10}\text{B}(n, \alpha_0)^7\text{Li}$ and $^{10}\text{B}(n, \alpha)^7\text{Li}$ reactions available in the EXFOR library [4], the present results are in good overall agreement with those reported by Haoyu Jiang (2019) [7]. In comparison, the present results exhibit more systematic behavior and smaller uncertainties, particularly for the $^{10}\text{B}(n, \alpha_0)^7\text{Li}$ reaction, owing to improved statistics.

B. Angle-integrated cross sections

The present results of angle-integrated cross sections for the $^{10}\text{B}(n, \alpha_1)^7\text{Li}^*$, $^{10}\text{B}(n, \alpha_0)^7\text{Li}$ and $^{10}\text{B}(n, \alpha)^7\text{Li}$ reactions are shown in Figs. 10, 11 and 12, which are com-

pared with those from existing measurements and evaluations. The inset in the upper right corner of Figs. 10, 11 and 12 shows the enlarged views in the $0.1 \sim 3.0$ MeV region. The present results are in good agreement with the results from evaluation libraries, including ENDF/B-VIII.1 [21], ENDF/B-VII.1 [28], JEFF-3.3 [23], ROSFOND-3.1 [24], CENDL-3.2 [27] and JENDL-5.0 [29].

In the neutron energy range from 0.3 eV to 100 keV, where the excitation functions of these three reactions follow the $1/v$ law, the present angle-integrated cross sections agree well with the evaluation results. In this energy region, due to the s -wave states of α_1 partial ($\Gamma_{n(\text{C.M.})} = 0.77$ MeV and $\Gamma_{\alpha(\text{C.M.})} = 0.113$ MeV) have broader width compared with the α_0 partial width ($\Gamma_{\alpha(\text{C.M.})} = 0.001$ MeV) [30], the cross sections of the $^{10}\text{B}(n, \alpha_1)^7\text{Li}^*$ reaction are much bigger than those of the $^{10}\text{B}(n, \alpha_0)^7\text{Li}$ reaction. Compared with the results of Haoyu Jiang (2019) [7], the present cross sections do not exhibit oscillations as a function of the neutron energy and have smaller uncertainties, because the energy spectrum was measured using the ^6Li -Si monitor instead of using $^{235}\text{U}(n, f)$ reaction. Compared with the results of Haoyu Jiang (2019) [7], the present uncertainties of the cross sections reduce

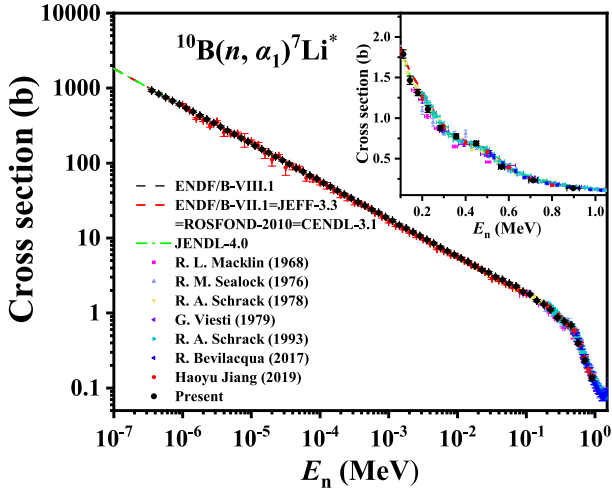


Fig. 10. (color online) Angle-integrated cross sections of the $^{10}\text{B}(n, \alpha_1)^7\text{Li}^*$ reaction compared with existing results of evaluations and measurements [4, 21, 23, 24, 27, 28, 29].

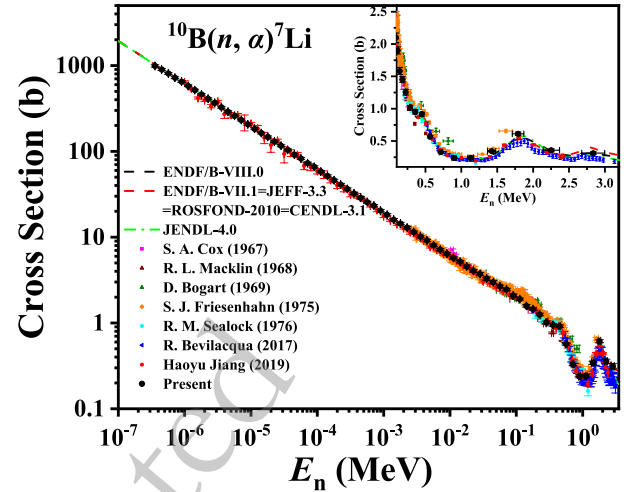


Fig. 12. (color online) Angle-integrated cross sections of the $^{10}\text{B}(n, \alpha)^7\text{Li}$ reaction compared with existing results of evaluations and measurements [4, 21, 23, 24, 27, 28, 29].

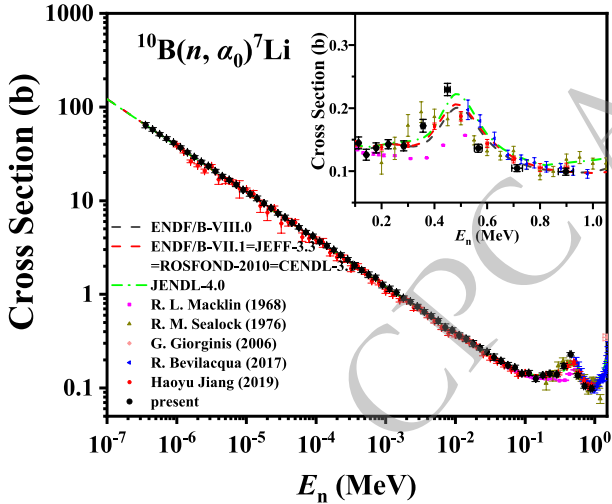


Fig. 11. (color online) Angle-integrated cross sections of the $^{10}\text{B}(n, \alpha_0)^7\text{Li}$ reaction compared with existing results of evaluations and measurements [4, 21, 23, 24, 27, 28, 29].

from 2.2% ~ 21.6% to 2.0% ~ 7.6%. In the experiment of Haoyu Jiang (2019) [7], the neutron energy spectrum was measured using a multi-layer fission chamber, which are based on the cross sections of the $^{235}\text{U}(n, f)$ reaction [12]. The cross sections of the $^{235}\text{U}(n, f)$ reaction exhibit dense resonances structure in the neutron energy region below 100 keV. On the contrary, the cross sections of the $^6\text{Li}(n, t)^4\text{He}$ reaction follow the $1/\nu$ law without significant resonance structures in the same neutron energy range. Thus, in the neutron energy region below 100 keV, the uncertainties of the present neutron energy spectrum measured using the ^6Li -Si monitor are smaller.

In the neutron energy region from 100 keV to 1 MeV, the excitation functions of these three reactions do not follow the $1/\nu$ law anymore. In the 0.5 ~ 1.0 MeV, the

angle-integrated cross sections of the $^{10}\text{B}(n, \alpha_1)^7\text{Li}^*$ and $^{10}\text{B}(n, \alpha)^7\text{Li}$ reactions exhibits a trend of rapid decline, as shown in Figs. 10 and 12. Conversely, the angle-integrated cross sections of the $^{10}\text{B}(n, \alpha_0)^7\text{Li}$ cross section have an observed resonance peak in the 300 keV – 600 keV region, due to the effect of $5/2^-$ p -wave ($E_n \sim 0.52$ MeV) resonance [30], as shown in Fig. 11. This resonance state significantly increases the $^{10}\text{B}(n, \alpha_0)^7\text{Li}$ cross sections, and lead to a rapid decrease in the $^{10}\text{B}(n, \alpha_1)^7\text{Li}^*$ cross sections above 500 keV. The angle-integrated cross sections of the $^{10}\text{B}(n, \alpha_1)^7\text{Li}^*$ and $^{10}\text{B}(n, \alpha)^7\text{Li}$ reactions are consistent with the evaluation data. However, the present angle-integrated cross sections of the $^{10}\text{B}(n, \alpha_0)^7\text{Li}$ reaction are higher at $E_n < 0.5$ MeV and lower at $E_n > 0.5$ MeV than the data of evaluations and other measurements. Compared with existing measurement data, the present cross sections of the $^{10}\text{B}(n, \alpha)^7\text{Li}$ reaction are closer to the results of Haoyu Jiang (2019) [7], and lower than those of Friesenhahn (1975) [31].

In the neutron energy region from 1.0 MeV to 3.0 MeV, the present results show the resonance effect in the excitation function of the $^{10}\text{B}(n, \alpha)^7\text{Li}$ reaction near $E_n \sim 1.8$ MeV, which might be contributed from the $9/2^-$ p -wave state ($E_n = 1.83$ MeV) and $5/2^+$ or $7/2^+$ d -wave state ($E_n = 1.88$ MeV) of the compound nucleus ^{11}B [32], as shown in Fig. 12. The angle-integrated cross sections of the $^{10}\text{B}(n, \alpha)^7\text{Li}$ reaction remain consistent with the results of Haoyu Jiang (2019) [7] and the evaluations, and they are lower than those of Friesenhahn (1975) [31] and higher than those of Hausladen (2017) [33].

V. CONCLUSIONS

In the present work, differential cross sections for the $^{10}\text{B}(n, \alpha)^7\text{Li}$ reaction have been measured using LPDA

detector system at 13 angles from 20.2° to 158.7° in the neutron energy from 0.3 eV to 3.0 MeV with 10 bpd (70 energy points). Differential cross sections for the $^{10}\text{B}(n, \alpha_0)^7\text{Li}$ and $^{10}\text{B}(n, \alpha_1)^7\text{Li}^*$ reactions have also been measured at the same angular positions in the neutron energy region from 0.3 eV to 1.0 MeV with 10 bpd (65 energy points). With the Legendre polynomial series fitting and integration, the angle-integrated cross sections for these three reactions have been obtained in the corresponding neutron energy region. In the neutron energy region from 0.3 eV to 100 keV, the present differential cross sections of the $^{10}\text{B}(n, \alpha_1)^7\text{Li}^*$, $^{10}\text{B}(n, \alpha_0)^7\text{Li}$ and $^{10}\text{B}(n, \alpha)^7\text{Li}$ reactions exhibit a nearly isotropic distribution in the center-of-mass system, and a slight forward bias emerges in the laboratory system as neutron energy increases. In the neutron energy region from 300 keV to 600 keV, the present differential cross sections of the $^{10}\text{B}(n, \alpha_0)^7\text{Li}$ reaction show a strong backward trend, consistent with our previous results (Haoyu Jiang, 2019). In the neutron energy region from 100 keV to 1 MeV, the forward trend of the $^{10}\text{B}(n, \alpha_1)^7\text{Li}^*$ differential cross sections in the present result is weaker than that in the evaluations, which also

agree with our previous measurement results (Haoyu Jiang, 2019). In the neutron energy from 1.0 MeV to 3.0 MeV, the present differential cross sections of the $^{10}\text{B}(n, \alpha_0)^7\text{Li}$ reaction exhibit significant forward-peak shape. The present angle-integrated cross sections of these three reactions generally agree with most of the results of evaluations and previous measurements, with minor deviations noted for the $^{10}\text{B}(n, \alpha_0)^7\text{Li}$ reaction from 0.3 to 0.6 MeV. Compared with other measurement results, the present results have lower uncertainties in the neutron energy region from 0.3 eV to 100 keV. Compared with our previous measurement results (Haoyu Jiang, 2019), the present results have been improved by resolving the issues of the energy spectrum oscillation in the low-energy region, improving measurement statistics, and expanding the measured energy range.

ACKNOWLEDGEMENT

The staff of the Back-n white neutron source facility (<https://cstr.cn/31113.02.CSNS.Back-n>) at China Spallation Neutron Source (CSNS) is acknowledged for providing stable neutron beam and technical support.

References

- [1] R. Bevilacqua *et al.*, *Nucl. Data Sheets* **119**, 104 (2014).
- [2] F. J. Hamsch and I. Ruskov, *Nucl. Sci. Eng.* **163**, 1 (2009).
- [3] A. D. Carlson *et al.*, *Nucl. Data Sheets* **148**, 143 (2018).
- [4] V. V. Zerkov and B. Pritychenko, *Nucl. Instrum. Meth. Phys. Res. A* **888**, 31 (2018).
- [5] R. M. Sealock and J. C., *Phys. Rev. C* **13**, 2149 (1976).
- [6] M. L. Stelts, *et al.*, *Phys. Rev. C* **19**, 1159 (1979).
- [7] H. Jiang, *et al.*, *Chin. Phys. C* **43**, 124002 (2019).
- [8] T. N. Massey, J. E. O'Donnell, J. Ralston, S. M. Grimes, *Phys. Rev. C* **105**, 054612 (2022).
- [9] H. Chen and X. L. Wang, *Nature Mater* **15**, 689 (2016).
- [10] J. Y. Tang *et al.*, *Nucl. Sci. Tech.* **32**, 11 (2021).
- [11] Q. An *et al.*, *J. Inst.* **12**, P07022 (2017). <https://doi.org/10.1088/1748-0221/12/07/P07022>.
- [12] H. Bai *et al.*, *Chin. Phys. C* **44**, 014003 (2020).
- [13] J. Liu *et al.*, *Eur. Phys. J. A* **59**, 106 (2023).
- [14] H. T. Jing *et al.*, *Nucl. Instrum. Meth. Phys. Res. A* **621**, 91 (2010).
- [15] L. Y. Zhang *et al.*, *Applied Radiation and Isotopes* **132**, 212 (2018).
- [16] H. Yi *et al.*, *J. Inst.* **15**, P03026 (2020). <https://doi.org/10.1088/1748-0221/15/03/P03026>.
- [17] Q. Li *et al.*, *Nucl. Instrum. Meth. Phys. Res. A* **946**, 162497 (2019).
- [18] K. Sun *et al.*, *J. Inst.* **18**, P04004 (2023). <https://doi.org/10.1088/1748-0221/18/04/P04004>.
- [19] S. Agostinelli *et al.*, *Nucl. Instrum. Meth. Phys. Res. A* **506**, 250 (2003).
- [20] B. He, P. Cao *et al.*, *Chin. Phys. C* **41**, 016104 (2017).
- [21] ENDF/B-VIII. 1, <https://www.osti.gov/biblio/2571019>. <https://doi.org/10.11578/ndf/257101922>.
- [22] Q. Li *et al.*, *Nucl. Instrum. Meth. Phys. Res. A* **980**, 164506 (2020).
- [23] A. J. M. Plompen *et al.*, *Eur. Phys. J. A* **56**, 181 (2020).
- [24] BROND-3.1, <https://vant.ippe.ru/en/>, retrieved 1st February 2026.
- [25] Y. Chen *et al.*, *Eur. Phys. J. A* **60**, 63 (2024).
- [26] Y. Chen *et al.*, *Eur. Phys. J. A* **55**, 115 (2019).
- [27] Z. Ge *et al.*, *EPJ Web Conf.* **239**, 09001 (2020).
- [28] M. B. Chadwick *et al.*, *Data, Nucl. Data Sheets* **112**, 2887 (2011).
- [29] O. Iwamoto *et al.*, *Journal of Nuclear Science and Technology* **60**, 1 (2023).
- [30] S. L. Hausladen, *et al.*, *Phys. Rev. C* **5**, 277 (1972).
- [31] EXFOR data: <https://www-nds.iaea.org/exfor/servlet/X4sGetSubent?reqx=54377&subID=10303004&plus=1>, retrieved 1st February 2026.
- [32] S. L. Hausladen *et al.*, *Nucl. Phys. A* **217**, 563 (1973).
- [33] R. Bevilacqua, F. -J. Hamsch, *et al.*, *EPJ Web Conf.* **146**, 11010 (2017). <https://doi.org/10.1051/epjconf/201714611010>.